University of Pennsylvania
ScholarlyCommons

Departmental Papers (CBE)

Department of Chemical & Biomolecular Engineering

3-2-2010

Atomistic Analysis of Phase Segregation Patterning in Binary Thin Films Using Applied Mechanical Fields

Alex M. Nieves
University of Pennsylvania, nievesam@seas.upenn.edu

Vaclav Vitek
University of Pennsylvania, vitek@seas.upenn.edu

Talid Sinno
University of Pennsylvania, talid@seas.upenn.edu

Follow this and additional works at: http://repository.upenn.edu/cbe_papers

Part of the Biochemical and Biomolecular Engineering Commons

Atomistic Analysis of Phase Segregation Patterning in Binary Thin Films Using Applied Mechanical Fields

Abstract

The patterned compositional evolution in thin films of a binary alloy controlled by modulated stress fields is studied by employing Monte Carlo simulations. General features of stress-patterned phase segregation are probed using a binary Lennard-Jones potential in which the lattice misfit between the two components of the alloy is varied systematically. In general, patterning of the microstructure is found to be more robust in the low-mismatch binary systems because large lattice mismatch promotes plastic, and therefore, irreversible relaxation, during annealing. It is shown that some control over the relaxation process can be achieved by careful design of the applied thermal annealing history. Additional calculations have been performed using two other potentials for binary metallic systems, an embedded-atom method (EAM) potential for Cu–Ag and a modified embedded-atom method (MEAM) potential for Cu–Ni that represent examples of high and low-mismatched systems, respectively. The results obtained with generic Lennard-Jones potentials are in excellent agreement with those from the EAM and MEAM potentials suggesting that it is possible to derive general guidelines for accomplishing stress-patterned segregation in a variety of thin films of binary alloys.

Disciplines

Biochemical and Biomolecular Engineering | Chemical Engineering | Engineering

Atomistic analysis of phase segregation patterning in binary thin films using applied mechanical fields

Alex M. Nieves,[1] V. Vitek,[2] and T. Sinno[1,a)]

[1]*Department of Chemical and Biomolecular Engineering, University of Pennsylvania, Philadelphia, Pennsylvania 19104, USA*
[2]*Department of Materials Science and Engineering, University of Pennsylvania, Philadelphia, Pennsylvania 19104, USA*

The patterned compositional evolution in thin films of a binary alloy controlled by modulated stress fields is studied by employing Monte Carlo simulations. General features of stress-patterned phase segregation are probed using a binary Lennard-Jones potential in which the lattice misfit between the two components of the alloy is varied systematically. In general, patterning of the microstructure is found to be more robust in the low-mismatch binary systems because large lattice mismatch promotes plastic, and therefore, irreversible relaxation, during annealing. It is shown that some control over the relaxation process can be achieved by careful design of the applied thermal annealing history. Additional calculations have been performed using two other potentials for binary metallic systems, an embedded-atom method (EAM) potential for Cu–Ag and a modified embedded-atom method (MEAM) potential for Cu–Ni that represent examples of high and low-mismatched systems, respectively. The results obtained with generic Lennard-Jones potentials are in excellent agreement with those from the EAM and MEAM potentials suggesting that it is possible to derive general guidelines for accomplishing stress-patterned segregation in a variety of thin films of binary alloys. © *2010 American Institute of Physics.* [doi:10.1063/1.3309480]

I. INTRODUCTION

The ability to spatially direct and pattern microstructural evolution of materials on an atomic level, for example, by the formation of precipitates or spinodal decomposition within a binary solid solution, offers the possibility to create uniquely designed periodic structures. This represents a potential for building materials with interesting optical, electronic, magnetic, or mechanical properties. One avenue for achieving such patterning is through the use of externally applied fields (e.g., electric,[1] magnetic,[2,3] or mechanical[4–7]) that couple to the atomistic transport and thermodynamic properties of the binary alloy. In hard materials, applied stress fields are particularly attractive because they can be readily applied at small length scales in both bulk and surface settings.[4–7] In this paper we analyze the coupling between an externally applied stress field and atomic transport and aggregation by extensive atomic level simulations.

Several experimental studies have demonstrated the feasibility of such coupling and related patterning in both metals[4,5] and semiconductors.[6,7] While patterning of metallic systems offers potential routes for forming high-density information storage structures, nanoscale patterning in semiconductor systems may open up new avenues for fabrication of microelectronic devices at higher densities and lower cost than that achievable by conventional lithographic methods.[8] For example, in a pioneering study Hung *et al.*[6] fabricated a GaAs-based multilayer structure using molecular beam epitaxy, whereby a thin layer of GaAs containing an excess of

As atoms was sandwiched between two AlGaAs layers. Localized stress fields were generated within the sandwiched GaAs layer by introducing lattice-mismatched stripes of In-GaAs onto the heterostructure. Upon annealing, precipitates were found first to nucleate homogeneously within the sandwiched GaAs layer, but eventually coarsened preferentially in regions below the stressor stripes. The driving force for this phenomenon was principally the difference of the elastic moduli of the precipitates and the surrounding matrix. Similar events have been observed during island formation on surfaces. For example, Ohtake and Koguchi[7] showed that GaAs islands formed by the sequential deposition of Ga and As atoms onto an InAs/GaAs heterostructure were spatially patterned in accordance with the underlying network of misfit dislocations at the InAs/GaAs interface that imparted a periodic strain field at the surface. Finally, strain-directed patterning is also found in systems that are strained intrinsically (i.e., do not contain an externally engineered strain source). For example, Pohl *et al.*[9] found that a silver submonolayer deposited onto a clean ruthenium (0001) surface spontaneously patterned into a monolayer honeycomb lattice of vacancy islands surrounded by a silver atomic network. This patterning resulted from the large lattice mismatch (approximately 7%) between Ag and Ru atoms that provided a surface-wide driving force for reorganization into the minimum energy patterned structure.

The complex interplay between atomic diffusion, phase segregation, and externally applied fields is ideally suited for study by simulation. A variety of modeling techniques have been applied in previous studies of directed assembly, ranging from fully atomistic methods such as Metropolis Monte Carlo (MC)[10,11] to rigid-lattice models such as kinetic

---

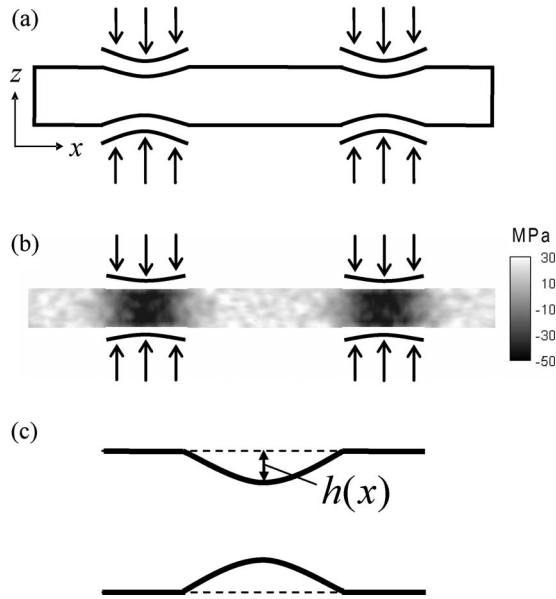a)Author to whom correspondence should be addressed. Electronic mail: talid@seas.upenn.edu.

FIG. 1. (a) Schematic representation of the xz-cross section of the simulation domain showing cylindrical intenders applied at top and bottom surfaces. (b) Instantaneous hydrostatic stress field within an xz-cross section of the simulation domain for a binary solid-solution LJ system with $\delta=-3\%$, 30% B, and $T^*=0.25$. In the legend: black represents compression and white denotes tension; the pressures are given in MPa. (c) Cartoon representation of the indented region including a schematic plot of the value of the indentation height, $h(x)$.

MC,[12,13] to continuum approaches, in particular, the phase-field method[14,15] based on the original work of Cahn and Hilliard.[16] As in all material modeling, each of these approaches is limited in some way; atomistic models are limited in scope to very small length and time scales and also depend strongly on the quality of the interatomic potential used, while coarser models require substantial mechanistic and parametric input before predictive calculations can be made.

In this paper, we employ quasistatic Metropolis MC simulations to study the kinematics and final equilibrium state of phase segregation in a thin film of a binary alloy subjected to a periodic strain field imposed by an array of cylindrical indenters that are applied to the film surface as shown in Fig. 1(a). The coupling between atomic evolution and the applied strain field is generated by introducing a size mismatch between the two types of atoms in the film; the smaller species are then attracted to the compressively stressed regions immediately below the indenters. Atomic diffusion in the binary system is modeled by identity switches between neighboring particles, which is assumed to implicitly capture transport via vacancy diffusion in real metallic systems while allowing for computationally efficient simulations. Global lattice relaxation during the simulation is achieved by periodic energy minimizations of the entire simulation cell. We consider various model binary material systems within the Lennard-Jones (LJ) representation by systematically varying the lattice mismatch between the two atomic components. We also consider two more realistic models for binary metallic systems: (1) an embedded-atom method (EAM) potential for Cu–Ag[17] and (2) a modified

EAM (MEAM) potential for Cu–Ni.[18] These two binary metallic systems represent both high (Cu–Ag) and low (Cu–Ni) lattice mismatch.

The remainder of the paper is organized as follows. In Sec. II, we present a description of the three potentials, LJ, EAM, and MEAM, used in this study. In Sec. III, the methodology of the calculation of phase diagrams and results for the LJ models with misfit of −3%, −7%, and −11% are discussed. Phase segregation simulations based on the LJ potential are presented in Sec. IV. In Sec. V, the segregation patterning within the Cu–Ag EAM model (∼11% misfit) and the Cu–Ni MEAM model (∼3% misfit) are presented and compared with the results of LJ simulations at similar lattice mismatches. Finally, in Sec. VI, we summarize the whole study, and based on the results, we derive guidelines for material selection and process conditions that are necessary to achieve stress-directed compositional patterning in films of binary alloys.

II. INTERATOMIC POTENTIALS

The binary LJ potential is first employed to investigate qualitatively the effect of lattice misfit on patterning mediated by phase segregation in generic fcc crystalline solids. An EAM potential for Cu–Ag alloy and a MEAM potential for Cu–Ni alloy are then applied for more specific analyses of binary metallic systems. In particular, the Cu–Ag system represents a high lattice-mismatch alloy (∼11%), while the Cu–Ni system is an example of a relatively low-mismatch case (∼3%). Details of these potentials are provided below.

A. Binary LJ

For two atomic species "A" and "B," the LJ interaction energy between atoms i and j separated by a distance r_{ij} is

$$E(r_{ij}) = 4\varepsilon_{SiSj}\left[\left(\frac{\sigma_{SiSj}}{r_{ij}}\right)^{12} - \left(\frac{\sigma_{SiSj}}{r_{ij}}\right)^{6}\right], \qquad (1)$$

where S_i is the species type of atom i, ε_{SiSj} is the energy parameter for the S_i-S_j interaction, and σ_{SiSj} is the length parameter for this interaction. The value of the energy and length parameters for the three possible interactions in a binary alloy ("A-A," "A-B," and "B-B") can be adjusted to create a desired lattice misfit and energy of the interface between the two species. The lattice misfit δ is defined by[19]

$$\delta = \frac{a_B - a_A}{a_A}, \qquad (2)$$

where a_i is the lattice parameter of the fcc crystal comprised of pure species i. Lattice misfit is introduced by making the length parameter for the B-B interaction smaller (negative misfit) or larger (positive misfit) than the A-A interaction, i.e., $\sigma_{BB}=(1+\delta)\sigma_{AA}$. The length parameter for A-B interactions is assumed to be the arithmetic mean of the A-A and the B-B length parameters, i.e., $\sigma_{AB}=(\sigma_{AA}+\sigma_{BB})/2$.

In general, the different effective atomic sizes in a mismatched binary system lead to an effective interface energy penalty between phases of different compositions. We introduce an additional (adjustable) parameter, γ', that controls the interface energy by setting the energy parameters for the

A-A and B-B interactions to be the same, $\varepsilon_{AA}=\varepsilon_{BB}$, and reducing the A-B interaction so that $\varepsilon_{AB}=(1-\gamma')\sqrt{\varepsilon_{AA}\varepsilon_{BB}}$. Reducing the A-B interaction energy relative to that of the A-A and B-B interaction energies penalizes A-B bonds and increases the driving force for phase segregation. For all simulations discussed in the subsequent sections we use $\varepsilon_{AA}=\varepsilon_{BB}=0.010\ 323$ eV and $\sigma_{AA}=3.405$ Å. The remaining three parameters are for each case determined according to the desired misfit and interface energy penalty. The parameter controlling the interface energy is set to a fixed value of $\gamma'=0.05$ for the three binary LJ systems studied in the present work. This choice of the value of γ' reduces the miscibility of the binary system at a given lattice mismatch and allows for phase segregation at higher simulation temperatures. The cutoff distance for all atomic interactions (r_c) in the LJ model was set to $r_c=2.2\sigma_{S_iS_j}$ and a third-order polynomial tail starting at $r_t=0.95r_c$ was employed to zero the energy and its derivative at r_c. All temperatures reported in the ensuing discussion of LJ simulation results are scaled by $T^*=T(k_B/\varepsilon_{AA})$, where k_B is the Boltzmann constant.

B. EAM potential for Cu–Ag

The EAM is an empirical scheme that has been used to model many studies of surfaces and defects in metallic systems.[20] Within the EAM framework, every atom is viewed as being embedded in a host system that consists of all surrounding atoms. The total energy of the system is given by

$$E_{tot} = \sum_i \left[F_i(\bar{\rho}_i) + \frac{1}{2}\sum_{j\neq i} \phi_{ij}(r_{ij}) \right]. \qquad (3)$$

Here ϕ_{ij} is the pair interaction energy between atoms i and j that are separated by r_{ij} and F_i is the embedding energy function for atom i, which depends on the empirically fitted function $\bar{\rho}_i$ that represents the host electron density at the location of atom i. A detailed description of the EAM functions and the fitting procedure used to model the Cu–Ag alloy employed here is given in Refs. 17 and 21. For the Cu–Cu and Ag–Ag interactions, the parameters used in the functions $\phi_{ij}(r_{ij})$ and $F_i(\bar{\rho}_i)$ are fitted to reproduce exactly the experimental fcc lattice parameter, the bulk modulus, and the cohesive energy for pure Cu and Ag, respectively. These parameters are also fitted to several experimental and *ab initio* calculated data including elastic moduli, relaxed vacancy formation energy, relaxed vacancy migration energy, and intrinsic stacking-fault energy. Defining Cu as the minority species B, the lattice mismatch for this system is -11.6%.

C. Modified embedded-atom potential for Cu–Ni

Within the EAM, $\bar{\rho}_i$ is assumed to depend only on the separation of atoms and thus possess spherical symmetry. The MEAM introduces an angular contribution to augment the spherically symmetric contribution within the EAM.[22] A detailed description of the parametrization and functions for the pure Cu and Ni components is presented by Lee *et al.*,[23] while the Cu–Ni interaction is given by Lee and Shim.[18] Within the MEAM, the total energy is given by

$$E_{tot} = \sum_i \left[F_i(\bar{\rho}_i) + \frac{1}{2}\sum_{j\neq i} \phi_{ij}(r_{ij})S_{ij} \right], \qquad (4)$$

where S_{ij} is a screening function ($0 \leq S_{ij} \leq 1$) and

$$\bar{\rho}_i = \rho_i^{(0)} \cdot \frac{2}{1 + \exp(-\Gamma_i)}, \qquad (5)$$

where

$$\Gamma_i = \sum_{h=1}^{3} t_i^{(h)}[\rho_i^{(h)}/\rho_i^{(0)}]^2, \qquad (6)$$

and $\rho_i^{(0)}$ is the spherically symmetric contribution, $\rho_i^{(1)}$, $\rho_i^{(2)}$, and $\rho_i^{(3)}$ are the angular contributions, and $t_i^{(1)}$, $t_i^{(2)}$, and $t_i^{(1)}$ are fitting parameters. Defining Ni as the minority species B, the mismatch for this system is -2.5%.

III. EQUILIBRIUM PHASE DIAGRAM CALCULATIONS (LJ)

The binary LJ interaction models applied in this work generally produce phase diagrams that contain a miscibility gap within the solid phase. At compositions and temperatures inside this miscibility gap, atoms in the binary system will segregate into two phases with compositions specified by the bounding *solvus* line. The miscibility gap may or may not intersect with liquid-solid coexistence regions that are delineated by the *solidus* and *liquidus* lines on the phase diagram. Obviously, any annealing process applied in practice to produce phase segregation in a binary system must be performed at sufficiently low temperatures so as to avoid any melting. In the following discussion, we describe methods for computing the location of the two-phase miscibility gap, as well as the locations of the *solidus* and *liquidus* curves for each of the three binary LJ cases considered in this paper, i.e., containing lattice misfits of -3%, -7%, and -11%.

A. Zero-stress semigrand canonical MC

Zero-stress semigrand canonical MC (SG-MC) simulations were used to calculate the miscibility gap and the solid-liquid coexistence regions. In this ensemble, the temperature (T), number of particles (N), and the difference in the chemical potential between the two species ($\Delta\mu \equiv \mu_B - \mu_A$) are all fixed, while the chemical identity (A or B) of each individual atom is allowed to change randomly. The SG-MC acceptance criterion for the change in identity is given by

$$P_{accept}(S_i^{old} \rightarrow S_i^{new}) = \min(1, \exp[-\beta[\Delta U(S_i^{old} \rightarrow S_i^{new})$$
$$- \xi\Delta\mu]]), \qquad (7)$$

where S_i^{old} is the old (current) species of atom i, S_i^{new} is the new (proposed) species of atom i, $\beta = 1/k_BT$, and $\Delta U(S_i^{old} \rightarrow S_i^{new})$ is the change in the potential energy due to the identity change of atom i. Identity changes are defined so that $\xi=1$ for an $A \rightarrow B$ identity change and $\xi=-1$ for a $B \rightarrow A$ one. Additional changes in the dimensions of the simulation box are applied in the x, y, and z directions (i.e., $\langle 100 \rangle$ directions)[17,18] to keep the tension/compression in each direction at zero. A change in the one of the box dimensions leads to a change in the volume of the system, and the acceptance criterion for

this type of move in zero-stress Metropolis MC is given by

$$P_{\text{accept}}(V^{\text{old}} \rightarrow V^{\text{new}}) = \min\left(1, \left(\frac{V^{\text{new}}}{V^{\text{old}}}\right)^N\right.$$

$$\left. \times \exp\{-\beta[\Delta U(V^{\text{old}} \rightarrow V^{\text{new}})]\}\right),$$

(8)

where V^{old} is the old (current) volume, V^{new} is the new (proposed) volume, N is the total number of atoms in the system, and $\Delta U(V^{\text{old}} \rightarrow V^{\text{new}})$ is the difference in potential energy due to the attempted change in volume.

B. *Solvus* line calculation

Within the zero-stress SG-MC method, the equilibrium composition of a binary material at a given T is determined by $\Delta\mu$. In the following discussion, the composition is defined by the atomic fraction of B, i.e., $X_B = N_B/(N_A + N_B)$, where N_i is the number of atoms of species i and $N_A + N_B = N$, the total number of particles. Within the solid-phase region of the phase diagram, a miscibility gap is indicated by a discontinuity in the computed value of X_B as a function of $\Delta\mu$. The two compositions at the point of discontinuity define the position of the *solvus* line at a given T. The two phase region is comprised of a solid-solution phase with lower B composition (α matrix phase), in addition to a solid-solution phase with higher B composition (β precipitate phase).

SG-MC simulations have been employed extensively for the calculation of *solvus* line positions[17,18] in binary solids. In the approach used in this work, each SG-MC simulation employed a periodic cubic domain consisting of 1372 atoms arranged in a perfect fcc lattice. The solid-phase SG-MC simulations were performed using a quasistatic simulation approach in which thermal vibrations (i.e., random atomic displacement attempts) are ignored and only volume and identity switch moves are considered. This approximation was used to ensure consistency with the kinetic simulations discussed in Sec. IV. Although the quasistatic assumption does affect the phase diagram, the differences are only quantitative and the overall shape of the miscibility gap within the solid is unaffected.

Within the quasistatic approach used in this work, each identity switch attempt is coupled with local relaxations of the lattice in the vicinity of the test atom so that the potential energies of the relaxed configurations before and after switch enter Eq. (7). All local relaxations were performed using a conjugate gradient method.[24] Note that if the identity switch move is accepted, the particle positions are updated with the new (locally) relaxed positions but otherwise the system configuration is unaltered. The radius of the minimum required relaxation sphere was determined using convergence studies for each of the three binary LJ potentials considered; $1.6r_c$ was sufficient for the $\delta = -3\%$ system, while $1.8r_c$ was required for the $\delta = -7\%$ and $\delta = -11\%$ systems.

The location of the *solvus* at each temperature was determined by performing a sequence of quasistatic SG-MC simulations in which the initial composition of the system was chosen to be in the miscibility gap. At a given temperature, the equilibrium system composition was mapped as a function of $\Delta\mu$. The location of the *solvus* line was found by performing simulations with increasing $\Delta\mu$ and monitoring the system for a discontinuity in X_B. In order to ensure that the initial composition was indeed located inside the miscibility gap, the first set of *solvus* points were calculated at sufficiently low temperatures so that the α phase was essentially 100% A and the β phase was 100% B. These simulations were started with an initial composition of 50%. After finding the two compositions of the solvus line at this low temperature, the temperature was increased and the above process repeated. At every new temperature, the initial composition was taken as the average of the two *solvus* compositions corresponding to the previous (lower) temperature. Starting inside the miscibility gap appears to reduce hysteresis in the plot of $\Delta\mu$ versus X_B, which has been observed in previous studies[17,18] where two simulations at a given $\Delta\mu$ and temperature were used to calculate the miscibility gap, one starting from pure A composition and the other from pure B. Moreover, initializing simulations inside the miscibility gap allows for the determination of both solvus compositions with a single scan in chemical potential values at a given temperature.

C. Solidus and liquidus line calculations

The *solidus* and *liquidus* calculation method used here is taken from Williams *et al.*[17] A simulation box {width-to-length-to-height ($x:y:z$) ratio 20:7:7} consisting of 3920 atoms was used to create two solid-liquid interfaces, along the (100) plane by melting the middle section of the box. At a given temperature, the interface motion was monitored as $\Delta\mu$ was varied in increments of 0.0001 eV. The goal is to find a value of $\Delta\mu$ for which there is no interface motion, indicating that the liquid and solid phases are in equilibrium. At each $\Delta\mu$, the motion of the system interface was monitored for 1.0×10^6 sweeps (one sweep represents one switch attempt per particle) in order to find the $\Delta\mu$ that led to solid-liquid equilibrium. Note that at each temperature there are two equilibrium values of $\Delta\mu$, corresponding to the liquid-α phase coexistence and the liquid-β phase coexistence, respectively. Once the equilibrium $\Delta\mu$ values were obtained at a given temperature, two simulations, one starting from a solid at 0% B and the other from a liquid at 50% B, were used to calculate the *solidus* and *liquidus* points of the α phase. Similarly, two additional simulations, one starting from a solid at 100% B and the other with liquid at 50% B, were used to calculate the *solidus* and *liquidus* lines for the β phase.

For all solid-liquid coexistence simulations, the system was evolved with the zero-stress SG-MC ensemble described previously and with the addition of random displacement (thermalization) moves to the already mentioned identity exchange and volume moves. The computationally demanding method described above was only applied to the two highest misfit cases: $\delta = -7\%$ and $\delta = -11\%$. For the $\delta = -3\%$ system, where the *solidus* and *liquidus* are very close to each other and far away from the miscibility gap [see Fig. 2(a)], the
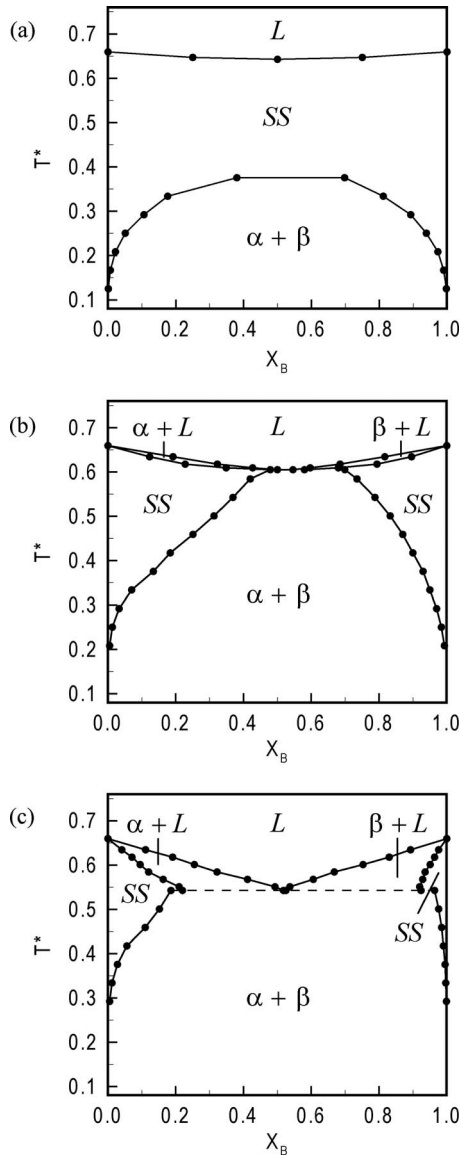
FIG. 2. The effects of the misfit on the form of the phase diagram of binary LJ materials. The misfits are (a) $\delta = -3\%$, (b) $\delta = -7\%$, and (c) $\delta = -11\%$. The marked regions in the phase diagrams are SS: solid solution, $\alpha + \beta$: two phase region, L: liquid phase, $L + \alpha$: liquid coexistence with solid α phase, and $L + \beta$: liquid coexistence with solid β phase.

solidus and *liquidus* lines both were approximated by the single constant-composition melting temperature at compositions of 0%, 25%, 50%, 75%, and 100%.

D. Binary LJ phase diagram results

Phase diagrams for the binary LJ systems with lattice misfits of -3%, -7%, and -11% are shown in Fig. 2. All three phase diagrams exhibit solid-solid miscibility gaps, with α and β phases, indicated by *solvus* lines. The shape of each *solvus* line changes as the value of δ varies. In general, the two atomic species become less miscible with increasing lattice mismatch, δ. As the lattice misfit increases, the larger A atoms become less soluble in the β phase at a faster rate than the B atoms in the α phase, which is represented by the steeper slope of the *solvus* line in the β region and flatter slope in the α region. The shape of the solid-liquid coexist-

ence regions is also affected by the variation in the lattice misfit; at -3% and -7% mismatches an azeotrope is formed, while at -11% mismatch a eutectic transformation takes place. It is also notable that the separation between *solidus* and *liquidus* lines increases with increasing misfit. These observations are consistent with the results of Hitchcock and Hall,[25] who studied the LJ binary potential with $\varepsilon_{AA} = \varepsilon_{AB} = \varepsilon_{BB}$ (i.e., $\gamma' = 0$). Hitchcock and Hall also showed that the minimum temperature at which the liquid phase is present decreases as lattice misfit increases, in agreement with the present calculations. Note that for the system with -3% misfit, a solid-solution phase exists at all compositions. As will be shown in the following sections, stress-directed patterning of phase segregation is dependent on access to a solid-solution region within the phase diagram. At higher misfits, the area of solid solution is reduced, thus limiting the overall system compositions that can be used for phase-segregation patterning.

Finally, the effect of the quasistatic assumption used in the solid-phase diagram calculations can be observed in Figs. 2(b) and 2(c). In particular, a deviation is seen for the compositions found at the intersection of the *solvus* line when employing the quasistatic method and *solidus* line measured using fully thermalized calculations. Although not relevant for the present study, it should be noted that the purely local relaxations employed in our solid-phase equilibrium simulations preclude the prediction of most noncubic crystal phases that may form in binary systems with very large lattice misfits.

IV. MC SIMULATION OF PHASE SEGREGATION UNDER APPLIED STRESS

The phase diagrams discussed in Sec. III were used to find appropriate initial conditions for MC simulations of phase segregation under applied stress. The latter simulations are also quasistatic but are designed to capture qualitative aspects of the kinetic evolution of phase segregation during annealing.

A. Simulation methods

The three-dimensional simulation domain employed throughout our study is shown schematically in Fig. 1(a). The total of 49 152 atoms, arranged in a fcc lattice, are present in the rectangular thin-film geometry {length-to-width-to-height $(x:y:z)$ ratio 128:8:12}. Standard periodic boundary conditions are applied in the x and y directions, while the two surfaces normal to z are subject to fixed strain in the z-direction. Note that in-plane relaxation of the surface atoms is permitted during the simulation. The system is initialized by random assignment of atomic identities to create a homogeneous solid solution with a specified composition in a perfect fcc lattice. The composition and initial system temperature are chosen such that the equilibrium state of the system is a solid solution as determined by the phase diagrams discussed in Sec. III. Next, two cylindrical indentations are created in each of the z-surfaces of the simulated thin film as shown in Fig. 1(a). This is achieved by displacing appropriately the surface atoms. The strain that arises

from the displacements of surface atoms is relaxed inside the film by minimizing the energy of the system using a conjugate gradient method. In the following simulations it is assumed that the thin film is freestanding except for contact with the indenters and therefore is maintained at zero total stress by coordinate rescaling moves in each of the three Cartesian directions. This approach naturally allows for thermal expansion/contraction during thermal annealing with varying temperature. An example of the hydrostatic stress field generated within a thin film by surface indenters is shown in Fig. 1(b) for a binary LJ system with B species fraction of 30% and $\delta = -3\%$ at T*=0.25. The regions just below the indenters are subjected to a compressive stress field, while away from the indenter the atoms experience some tension in order to satisfy the overall condition of zero stress.

The initialized system described above is evolved via atomic identity exchanges of two randomly chosen nearest-neighbor atoms. These local exchanges are accepted or rejected according to the standard Metropolis MC criterion at a prescribed temperature. The number of local identity switch attempts is used to monitor atomic evolution during the annealing process. It is reasonable to assume that identity exchanges of nearest-neighbors provide a coarse-grained representation of atomic diffusion. Although in real crystalline systems point defects act as the primary facilitating medium for such diffusion (e.g., vacancies in metals[26]); explicit consideration of this diffusion mechanism is not computationally feasible in the present studies. On the other hand, assuming that point defects are distributed uniformly throughout the domain (i.e., they are independent of composition and stress), the total number of local identity switches can be regarded as representing a qualitative measure of the temporal evolution. Note that even though same-type exchanges do not alter the system configuration, they are still counted toward the total number of switch attempts in order to preserve the proportionality between identity switches and temporal evolution.

The quasistatic nature of the present simulations dictates that the atomic coordinates be relaxed periodically because no thermalization moves are performed. This is accomplished with global energy minimizations. The necessary frequency of such minimizations was found to depend strongly on the lattice mismatch in the system. For example, in systems with low misfit where defects, such as faulted loops that produce plastic deformation are not generated, it is sufficient to relax the system every 100 sweeps. This was determined by comparing the system evolution to a reference simulation in which relaxation was performed at every sweep.[10] On the other hand, for a system with high misfit, more frequent relaxations are needed in order to capture the occurrence of plastic deformation within the lattice. Therefore, in the following simulations energy minimizations were performed every 100 sweeps for the low-mismatch LJ ($\delta = -3\%$) and the MEAM CuNi systems. For the medium and high mismatch LJ ($\delta = -7\%$ and $\delta = -11\%$, respectively) and the EAM CuAg systems, energy minimizations were performed every ten sweeps.
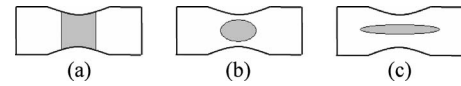

FIG. 3. Cartoon representation of three different patterns showing the quantitative effect of pattern shape in ψ. As shown here: $\psi_a > \psi_b > \psi_c$.

1. Order parameter definition

In order to capture quantitatively the extent of patterning during the segregation simulations, an order parameter (ψ) that represents the amount of B atoms in the indented region was defined as

$$\psi = \frac{\int_0^L C_B(x)h(x)dx}{\psi_{\max}}, \qquad (9)$$

where L is the length of the film in the x-direction, $C_B(x)$ is the concentration of B at position x, and $h(x)$ is the indentation height relative to the flat surface, Fig. 1(c). The system is divided into 128 bins of size $128/L$ along the x-direction and the B concentration in the bin k, $C_B(x=x_k)$, is given as $C_B(x_k)=N_B^k/N_T^k$, where N_B^k is the number of B atoms in bin k and N_T^k is the total number of atoms in bin k. The integral is calculated numerically using the trapezoid rule. By definition, the minimum ψ is zero, which is when all the B atoms are outside of the indented region. The order parameter ψ is normalized to unity using its maximum possible value, $\psi_{\max}$, which is given by

$$\psi_{\max} = \int_0^L C_B^{\max}(x)h(x)dx, \qquad (10)$$

where $C_B^{\max}(x)$ is defined such that all the B atoms for the given material composition are placed in the bin(s) with the largest height. $C_B^{\max}(x)$ is calculated by finding the bin with the maximum height and making all the atoms in that bin B type. After that (if there are B atoms remaining), the bin with the second largest height is filled with B atoms; this process is continued until all the B atoms in the system have been systematically assigned to the bins with the largest height. As defined, ψ depends on the equilibrium composition of the β phase dictated by the phase diagram, the location and shape of the precipitates in the film, and the indenter geometry. The maximum patterning extent, $\psi=1$, is only obtained for a pure B precipitate that is centered at the highest indenter depth and extends across the thickness of the film; examples are shown in Fig. 3 for several representative configurations.

B. Equilibrium precipitate shape as a function of lattice misfit

First, equilibrium precipitate shapes predicted by quasistatic MC simulations were characterized to ensure that the approach allows for sufficient relaxation to capture large-scale morphological evolution. Three quasistatic zero-stress MC simulations were performed at constant temperature in a periodic cubic box consisting of 13 500 atoms arranged within a fcc lattice with $X_B=0.1$. Binary LJ systems with lattice misfits of -3%, -7%, and -11% were held at temperatures of 0.167, 0.201, and 0.292, respectively. Previous studies have demonstrated that the shape of β phase precipi-
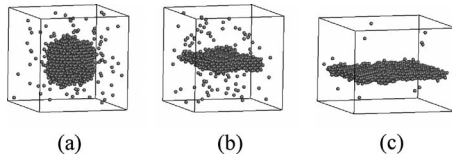
FIG. 4. Morphological change in β precipitates with increasing misfit: (a) $\delta = -3\%$, (b) $\delta = -7\%$, and (c) $\delta = -11\%$. Only B atoms are shown.

tates changes from spherical to platelike as the misfit between A and B species increases.[19,27] The precipitate shape is determined by a competition between interface and strain energies. When the interface energy dominates (small misfit), the system energy is minimized by the growth of a spherical precipitate, which reduces the surface area of the precipitate-matrix interface. When the strain energy dominates (high misfit), energy is minimized by the formation of a platelike precipitate phase which reduces the total strain in the system. As Fig. 4 shows, this behavior is captured in our simulations. For low misfit, -3%, the shape of the β precipitate is spherical and as the misfit increases to -7% and -11%, the precipitate becomes increasingly flat and more platelike.

C. Strain-directed patterning at low lattice misfit (-3%)

We consider first the low misfit case, $\delta = -3\%$, and perform two types of simulations. The phase diagram for this system, Fig. 2(a), shows that below $T^* = 0.167$, the precipitate phase has an equilibrium B concentration higher than 99%, while the matrix phase has an equilibrium B concentration lower than 1%. In the first simulation, we consider a binary thin-film initially comprised of 30% B atoms in a solid-solution configuration that is instantaneously quenched to a temperature of $T^* = 0.167$ (which is inside the miscibility gap region) and annealed at constant temperature. The second simulation was performed at variable temperature, starting at $T^* = 0.417$ (solid solution) for 3000 sweeps, followed by a linear temperature decrease (gradient $= -1.67 \times 10^{-5}$ scaled degrees per sweep) to the final holding temperature $T^* = 0.167$. The evolution of the order parameter for these two processes is shown in Fig. 5. Even though both pro-
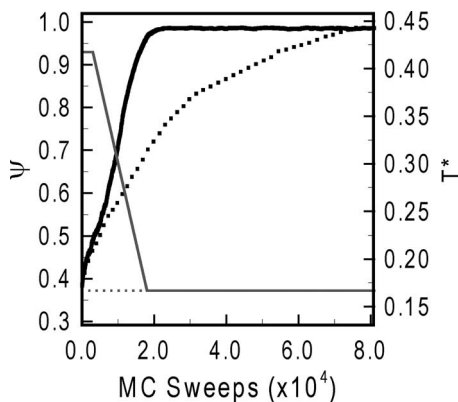

FIG. 5. Evolution of the order parameter ψ (thick lines) as a function of sweeps for constant temperature anneal at $T^* = 0.167$ (dotted line) and nonisothermal anneal with $0.167 \leq T^* \leq 0.417$ (solid line) for the LJ $\delta = -3\%$ binary system. The corresponding annealing temperature history for both simulations is also shown (thin lines).
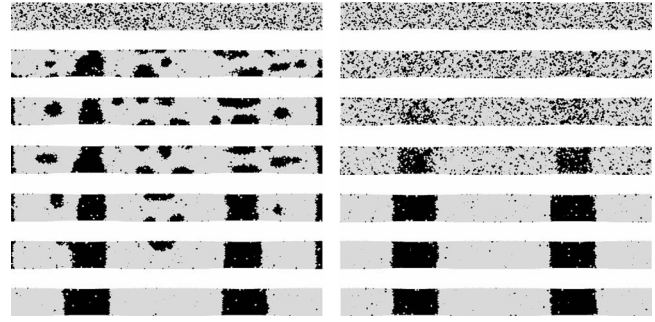

FIG. 6. Compositional evolution as a function of the total number of sweeps for the $T^* = 0.167$ isothermal (left column) and $0.167 \leq T^* \leq 0.417$ nonisothermal (right column) anneals for the LJ $\delta = -3\%$ binary system. A atoms are shown in light gray and B atoms in black. From top to bottom, the images on each row correspond to 0, 1000 ($T^* = 0.417$), 5000 ($T^* = 0.384$), 10 000 ($T^* = 0.301$), 18 000 ($T^* = 0.167$), 30 000 ($T^* = 0.167$), and 80 000 ($T^* = 0.167$) sweeps, respectively. The quoted temperatures correspond to the nonisothermal anneal history.

cesses eventually achieve complete patterning ($\psi \approx 1$), the nonisothermal process patterns the films at approximately one quarter of the sweeps it takes to pattern the film in the constant temperature process.

Figure 6 shows the morphological evolution within the film at a sequence of different times during both annealing processes. In the constant temperature process, precipitates nucleate instantaneously with the *solvus* composition of β phase at $T^* = 0.167$ (i.e., $X_B \sim 100\%$). Importantly, this nucleation process is strongly driven by the reduction in free energy that arises when the precipitates are grown from the solid-solution phase and is not biased appreciably by the presence of the indenters. Once the precipitates form, further compositional evolution within the film is mediated entirely by precipitate ripening.[10] It is during the latter process that patterning begins, thus requiring a lengthy anneal before full patterning is achieved. By contrast, in the nonisothermal process the driving force for nucleation is increased gradually as the system is driven into the two-phase region. Preferential diffusion of B atoms into the indented regions, mediated by the local compressive stress, maintains a reduced nucleation driving force in the nonindented regions. As a result, the system is essentially prevented from extensive nucleation of B-rich precipitates everywhere except in the regions below the indenters, where the B concentration is continuously increased. In other words, growth of large B-rich precipitates away from the indented areas is avoided by maintaining the composition there at a value close to the *solvus* composition at all times during the cooling process.[10] Note that the presence of a solid-solution phase at all compositions [Fig. 2(a)] allows for this patterning approach to be applied at any overall system composition.

The optimal annealing schedule that maximizes the rate and extent of patterning depends on the following factors: the details of the phase diagram for a particular material system, the composition and geometry of the thin film, and the size, shape, and pitch of the indenter array. In the following sections we focus on the effect of lattice mismatch, which we show to be a key factor in determining whether binary segregation patterning by applied stress can be achieved in realistic materials.
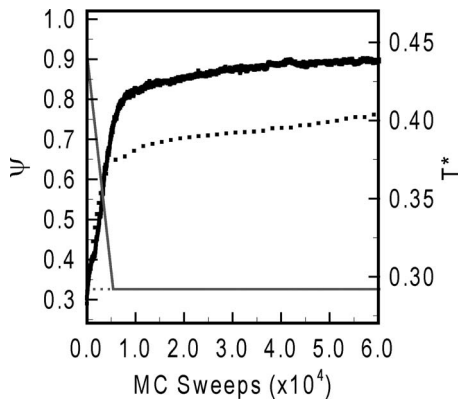
FIG. 7. Evolution of the order parameter ψ (thick lines) as a function of the number of sweeps for constant temperature anneal at T*=0.292 (dotted line) and nonisothermal anneal with $0.292 \leq T^* \leq 0.442$ (solid line) for the LJ δ =−11% binary system. The corresponding annealing temperature history for both simulations is also shown (thin lines).

D. Patterning at high misfit (−11%)

In highly mismatched alloys, the solid-solution regions within the phase diagram exist only for certain compositions, namely, those that are either highly A enriched or highly B enriched. For the −11% misfit LJ binary model, X_B=5% at T*=0.442 lies within a solid-solution region [see Fig. 2(c)] and was used as an initial condition for fabricating patterned films. Once again, two simulations starting with 5% B initialized into a solid-solution configuration were performed. In the first simulation, the system was immediately quenched to T*=0.292 and evolved under isothermal conditions, while in the second, nonisothermal annealing was applied in which the initial temperature was set to T*=0.442, which is just above the solvus temperature at X_B=5%. The annealing schedule included a linear temperature decrease to T* =0.292, with the gradient of -2.78×10^{-5} scaled degrees per sweep.

The evolution of the order parameter for these two processes is shown in Fig. 7. In both cases, it is no longer possible to achieve ψ=1 because of the platelike morphology of the precipitate phase at high mismatch. Nevertheless, the nonisothermal anneal is still able to reach a higher value of ψ in less sweeps than the constant temperature anneal, and both anneals are able to demonstrate a clear strain-directed patterning effect as in the low-mismatch case. Once again, the difference in evolution between the two cases arises from the fact that the isothermal case leads to precipitate nucleation throughout the domain, while the variable temperature anneal restricts nucleation to the regions below the indenters. The compositional distributions near the end of both anneals are shown in Fig. 8, clearly highlighting the platelike precipi-
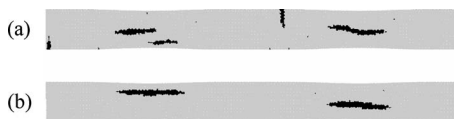

FIG. 8. Snapshot of compositional patterns at 50 000 sweeps for the LJ material with δ=−11% in (a) constant temperature anneal at T*=0.292 and (b) nonisothermal anneal with $0.292 \leq T^* \leq 0.442$. A atoms are light gray and B atoms black.
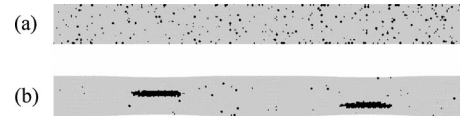

FIG. 9. Snapshot of compositional patterns in binary LJ film with δ= −11% in constant temperature anneal at T*=0.442 for (a) unindented film and (b) indented film. A atoms are colored light gray and B atoms black.

tate morphology. Also note that the residual vertical precipitates formed in the region between the indenters in the isothermal case [Fig. 8(a)]; these are extremely difficult to anneal out of the film once formed.

In the examples presented thus far, the temperature and composition of the binary film were chosen to drive the system into the two phase region. Here, we demonstrate another approach for achieving strain-directed patterning in highly mismatched systems. In this case, the initially homogenous system (X_B=5%) is annealed isothermally at T*=0.442. In the absence of indentation, it is expected that such a system would remain in the solid-solution phase according to the phase diagram in Fig. 2(c); this is indeed borne out in Fig. 9(a) that shows the film compositional distribution after 5000 sweeps. However, an interesting phenomenon is observed in Fig. 9(b) in which spatially patterned precipitates are observed under the indenters even though the phase diagram predicts a solid solution under these conditions. In this case, strain-driven diffusion of monomer B atoms into the indenter regions increases locally the concentration until species B become supersaturated and form precipitates even though the overall content of B species in the film is only 5%. This approach could be practically useful because it provides more robust control of precipitation throughout the film and there is no need for careful control of the annealing temperature in order to limit nucleation and growth throughout the film.

E. Patterning at intermediate misfit (−7%)

The final binary LJ system examined is one with an intermediate mismatch of −7% and an overall composition of X_B=30%. The constant temperature case was carried out at T*=0.25, while the nonisothermal simulation included a 2000-sweep hold at T*=0.543 followed by a linear decrease (gradient=-3.34×10^{-5} scaled degrees per sweep) to T* =0.25 at which the remainder of the anneal was performed. The evolution of ψ for these two processes is shown in Fig. 10. Notably, the achievable value of ψ is very different for the two cases, although both simulations appear to reach their apparent final values at approximately the same number of sweeps. The discrepancy is explained by the compositional distributions shown at the end of the variable temperature and isothermal processes in Figs. 11 and 12, respectively. The distribution at the end of the variable temperature process is unremarkable—the system has patterned fully into a distribution that closely resembles that of the δ=−3% case (i.e., $\psi \approx 1$). On the other hand, the case of the isothermal annealing shows a much more complex picture with clear evidence of plastic deformation within the precipitates lo-
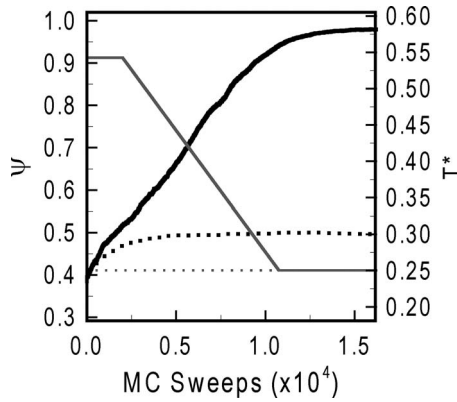
FIG. 10. Evolution of the order parameter ψ (thick lines) as a function of the number of sweeps for isothermal anneal at $T^*=0.25$ (dotted line) and non-isothermal anneal with $0.25 \leq T^* \leq 0.543$ (solid line) for the LJ $\delta=-7\%$ binary system. The corresponding annealing temperature history for both simulations is also shown (thin lines).

cated beneath the indenters. Upon close inspection, the defects shown in Fig. 12 are faulted loops of $1/6\langle 112 \rangle$ partial dislocations on {111} planes.

Also notable is the precipitate orientation within the film; precipitates located under the indenters are aligned horizontally, while those in the tensile regions are vertical. This effect was also observed in the −11% misfit case in Figs. 8 and 9 and agrees qualitatively with previous results.[28] In general, it has been shown that in the regions of compression the β precipitates align perpendicularly to the direction of the imposed compressive field but are parallel to it in the tensile regions away from the indenters. For example, using a continuum mechanics model, Li *et al.*[28] showed that the orientation of platelike θ-precipitates in an Al–Cu alloy can be controlled with the application of a unidirectional stress field.

The observation that annealing conditions not only vary the patterning rate but could also alter the threshold for the formation of plastic (irreversible) deformation deserves further study. Clearly, avoidance of plastic deformation during annealing would be highly desirable for the robust formation of patterned alloys because defects such as faulted loops are difficult to anneal out of the sample once formed. The formation energy of faulted loops lying on {111} planes can be estimated by summing over the contributions from the stacking fault and bounding partial dislocation, i.e.,

$$E_{FL}^f = \gamma_{SF}(\pi R^2) + E_{PDL}(2\pi R), \tag{11}$$

where R is the radius of the loop (assuming circular geometry), γ_{SF} is the stacking-fault energy per unit area, and E_{PDL}
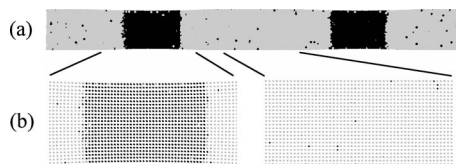

FIG. 11. (a) Compositional representation of the atomic configuration of the LJ $\delta=-7\%$ binary material at the end of the nonisothermal anneal with $0.25 \leq T^* \leq 0.543$. (b) Closeup views of (left) the atomic pattern formed in the left indented region of (a) and (right) the middle region between indenters of (a). A atoms are light gray and B atoms black.
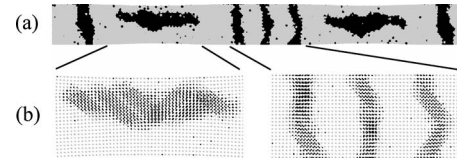

FIG. 12. (a) Compositional representation of the atomic configuration of the LJ $\delta=-7\%$ binary material at the end of the $T^*=0.25$ isothermal anneal. (b) Closeup view of (left) the precipitate shown in the left indented region of (a) that contains defects related to plastic deformation and (right) the stripes that form in the regions away from the indenters in (a) that also contain deformation related defects. A atoms are light gray and B atoms black.

is the elastic energy of the partial dislocation per unit length. The work (performed by the stress) required to expand a circular loop to a radius R is given by

$$W_{FL} = \tau b(\pi R^2), \tag{12}$$

where b is the magnitude of the Burgers vector of the partial dislocation and τ is the shear stress within the slip plane of the {111} type in the direction of the Burgers vector. Generally, in order for a loop of a given radius to be formed, the work made by the stress must be equal or larger than the formation energy, i.e., $W_{FL} \geq E_{FL}^f$. Combining Eqs. (11) and (12) provides a criterion for the formation of the faulted loop,

$$\tau_{crit} \geq \frac{\gamma_{SF}}{b} + \frac{2E_{PDL}}{bR}, \tag{13}$$

where τ_{crit} is the minimum shear stress for which a faulted-loop of radius R can be created. A reasonable estimate for the minimum loop radius (which requires the highest shear stress to form) is $R \sim 2\overline{a_0}$, where $\overline{a_0}$ is a representative lattice parameter. Substituting this value for the radius into Eq. (13) gives

$$\tau_{crit} \geq \frac{\gamma_{SF}}{b} + \frac{E_{PDL}}{ba_0}. \tag{14}$$

Equation (14) suggests two contributing factors to the explanation why faulted loops form during isothermal annealing at $T^*=0.25$ but not when the film is annealed with a gradual linear temperature decrease from $T^*=0.543$. One is that the maximum shear stress present in the isothermal case is larger and exceeds the critical value. This hypothesis was confirmed by calculating the maximum shear stress on the {111} planes in the $\langle 112 \rangle$ directions as a function of sweeps in the two simulations; details of the stress calculation method are provided in Appendix. Although, as shown in Fig. 13, the measured maximum shear stress is consistently lower in the nonisothermal process, the difference is only about 15%–20% in the interval before the onset of plastic deformation (dashed vertical line).

Another possible contributing factor is that the stacking-fault and/or the dislocation formation energies in the two cases vary due to differing compositional distributions of the segregating phases during annealing. The energy of the partial dislocation loop per unit length can be approximated as[29]
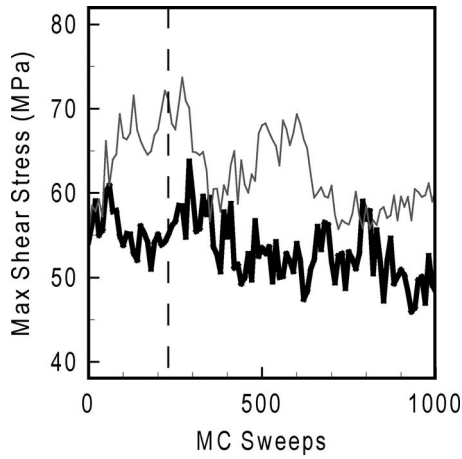
FIG. 13. Early stage evolution of the maximum shear stress on the {111} plane in the ⟨112⟩ direction measured before energy minimizations as a function of the number of sweeps for constant temperature anneal at T^* =0.250 (dotted line) and nonisothermal anneal with $0.543 \leq T^* \leq 0.250$ (solid line) for the LJ $\delta = -7\%$ binary system. The onset of the plastic deformation in the constant temperature anneal is marked by the horizontal dashed line.

$$E_{PDL} \sim \frac{G_{\{111\}}b^2}{4\pi}\ln\left(\frac{R}{b}\right), \tag{15}$$

where $G_{\{111\}}$ is the shear modulus in the {111} plane in the direction of the loop Burgers vector and is given by[30]

$$G_{\{111\}} = \frac{3C_{44}(C_{11}-C_{12})}{4C_{44}+C_{11}-C_{12}}. \tag{16}$$

C_{11}, C_{12}, and C_{44} are the elastic constants (moduli) for a cubic material with $C_{44}=C_{12}$ (the so-called Cauchy relation) valid for any pair potential. The elastic constants C_{11} and C_{12} were computed with a standard approach based on Hooke's law by applying unidirectional strain (e_{zz}) on a cubic simulation cell and then measuring the resulting stress, i.e.,

$$\tfrac{1}{2}(\sigma_{xx}+\sigma_{yy})=2C_{12}e_{zz}, \tag{17}$$

$$\sigma_{zz}=C_{11}e_{zz}, \tag{18}$$

where σ_{xx}, σ_{yy}, and σ_{zz} are the stress components normal to the x, y, and z directions, respectively. The estimated unrelaxed stacking-fault energy (γ_{SF}), shear modulus in the {111} plane, $G_{\{111\}}$, and τ_{crit} for pure A and pure B phases at zero temperature and stress are given in Table I. These values were also measured for a solid-solution phase with 30% B and for a material with pure α and β phases separated by an interface along the {111} plane. Although there is little

TABLE I. Properties of LJ binary material with −7% lattice misfit calculated at zero temperature and stress.

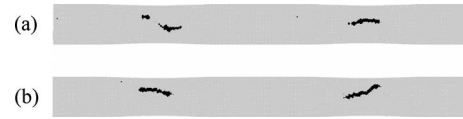|	γ_{SF} (mJ/m^2)	$G_{\{111\}}$ (MPa)	τ_{crit} (MPa)
α	0.88	1050	56
β	1.01	1310	73
Solid solution ($X_B=30\%$)	0.58	1100	60
Pure α/β Interface	−0.61	1160	57

FIG. 14. Compositional patterning in the Cu–Ag system with 2% Cu at (a) T=700 K and (b) $700 \leq T \leq 920$ K. Ag atoms are light gray and Cu atoms black.

change in the value of $G_{\{111\}}$ and τ_{crit} between the different cases, the stacking-fault energy indeed varies significantly, becoming negative along the pure α/β interface which characterizes the precipitate/matrix boundaries at low temperature. In other words, such precipitate boundaries are likely to be preferential sites for nucleating faulted loops.

Inserting the values from Table I into Eq. (14) and considering the difference in the maximum shear stresses shown in Fig. 13 indicates that the maximum shear stress during the nonisothermal anneal remains below τ_{crit}, while τ_{crit} is exceeded in the constant temperature anneal. Although the estimates provided here are only approximate and the stacking-fault contribution to the critical stress estimate is relatively small, it is clear that careful choice of annealing conditions can, in fact, play a role in inhibiting irreversible deformation that essentially halts any further patterning. This situation is likely to be most relevant in alloys with a medium misfit.

V. COMPARISONS WITH EAM AND MEAM MODELS

In this section, we compare various predictions obtained with the generic binary LJ simulations to those obtained using more realistic representations of binary metallic alloys, namely, EAM Cu–Ag and MEAM Cu–Ni. As discussed earlier in the paper, these two binary systems are examples of high and low-mismatched binary metallic alloys, respectively.

A. Cu–Ag EAM model

The large mismatch in the Cu–Ag alloy (∼11% misfit) leads to a qualitatively similar phase diagram to that shown in Fig. 2(c) for the $\delta=-11\%$ binary LJ model.[17] A total of three simulations initialized in the solid-solution phase with 2% Cu were used to study patterning response in the presence of cylindrical indenters. The first was an isothermal anneal at T=700 K, which lies within the two-phase envelope of the phase diagram generated in Ref. 17. The second simulation applied a variable temperature anneal beginning at T=920 K and decreasing linearly (gradient=−2.0 ×10^{-2} K per sweep) to T=700 K. As in the high-misfit LJ case (Fig. 7), the evolution within the variable temperature anneal run for the Cu–Ag system exhibited faster patterning than the constant temperature anneal. The final compositional distributions for both simulations are shown in Fig. 14; as in the LJ case, both anneals lead to platelike precipitates that are aligned perpendicularly to the direction of compression.

The third computational experiment was performed at a constant temperature of T=920 K which lies squarely within the solid-solution portion of the phase diagram. Once

FIG. 15. Compositional pattern in the Cu–Ag alloy in the constant temperature anneal at T=920 K for (a) a film with indentations and (b) a film with no indentations. Ag atoms are light gray and Cu atoms black.

again, precipitates are observed in the indenter region due to the strain-directed diffusion of Cu into the indenter region, providing further evidence for the viability of this approach. The final compositional distribution for this simulation is shown in Fig. 15(a). An identical run with no applied stress shows that the system remains in the solid-solution state, as previously observed in the high-misfit LJ case, see Fig. 15(b).

B. MEAM Cu–Ni model

The MEAM Cu–Ni system exhibits a lattice mismatch of −2.5% with Ni defined as the minority species. The phase diagram for this system (see Ref. 18) is qualitatively similar to that of the −3% misfit binary LJ model in that a solid-solution phase is present at all compositions. Two indentation simulations initialized in the solid-solution phase with 30% Ni were performed. In the first simulation a constant temperature anneal was applied at T=423 K (inside the miscibility gap region), while the other consisted of a nonisothermal anneal that started at T=700 K (in the solid-solution region) and decreased linearly to T=423 K at a rate of -2.86×10^{-2} K per sweep followed by a hold at T=423 K. The compositional evolutions in both simulations are shown in Fig. 16, in which it is readily apparent that behavior very similar to that found for the −3% misfit LJ case is produced. The evolution of the order parameter for these two processes also was qualitatively similar to that shown in the LJ system with −3% misfit (Fig. 5), although the maximum value of the order parameter in the Cu–Ni case was found to be 0.9. The incomplete patterning ($\psi = 0.9$) arises from the fact that at T=423 K both the matrix and the precipitate phases are
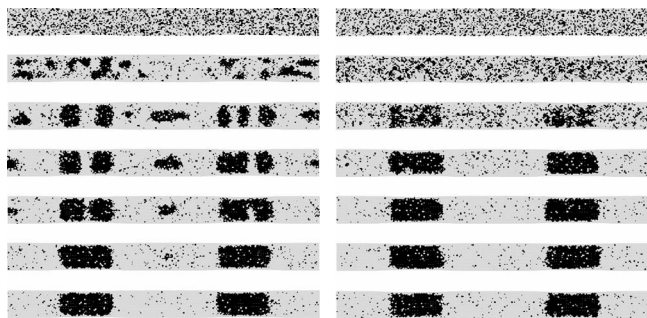

FIG. 16. Compositional evolution as a function of the total number of sweeps for the T=423 K isothermal (left column) and $423 \leq T \leq 700$ K nonisothermal (right column) anneals of Cu–Ni with 30% Ni composition, beginning from a homogeneous solid solution. Cu atoms are colored red (dark gray) and Ni atoms are colored green (light gray). From top to bottom the images on each row correspond to 0, 1000 (T=671 K), 5000 (T =557 K), 10 000 (T=423 K), 15 000 (T=423 K), 20 000 (T=432 K), and 25 000 (T=423 K) sweeps, respectively. The quoted temperatures correspond to the nonisothermal anneal.

not entirely pure. Although further decrease in the simulation temperature would increase the order parameter, it is likely that in practice the low atomic mobility at low temperature would be impractical for further patterning.

VI. CONCLUSIONS

An extensive simulation study of strain-directed phase segregation in binary alloy thin films was performed in which the smaller of two atomic species was driven into regions of compressive stress created by an array of indenters applied at the film surface. Two classes of empirical interatomic potentials were used in the study. In the first set of calculations, a binary LJ potential was parametrized to generate three model material systems with varying amounts of lattice mismatch between the two components, which produced qualitatively different phase diagrams. The results of the LJ calculations were then compared with those generated by EAM models for two binary metallic alloys, Cu–Ag and Cu–Ni, representing examples of high and low-mismatch cases, respectively. Overall, it is found that the LJ models are able to reproduce essentially all of the phase segregation behavior found in the EAM/MEAM studies for both the high and low-mismatch examples. As such, the observations and conclusions of this work appear to be generally applicable to a wide range of fcc-based alloys.

Generally, our results highlight a key issue for practical application of strain-directed phase segregation in thin films of binary alloys: access to a region of the phase diagram containing a solid solution. Although we are not able to directly estimate required annealing times with our MC-based approach, it is clear that patterning by ripening of already existing homogeneously distributed precipitates would require impractically long anneals. In all cases, patterning was achieved much more rapidly and robustly when the strain field was applied to a solid solution, thereby establishing much of the patterning before extensive precipitation took place throughout the sample.

Low misfit alloys, which exhibit a solid-solution region at all compositions, are therefore excellent candidates for the approach presented in this paper. The patterning efficiency in these materials was readily optimized with variable temperature annealing that gradually increases the driving force for segregation as the regions away from the indenters become increasingly depleted in the precipitating smaller species. Conversely, the components of high-misfit systems exhibit very limited mutual solubility. In this case, simulations with dilute alloys demonstrated that variable temperature annealing can still enhance the patterning process, although the resulting precipitate concentrations were obviously lower than in the low misfit case. Any attempt to pattern more concentrated films ($>5-10\%$ minority species) led to the rapid formation of homogeneously distributed precipitates.

The LJ alloy with a moderate mismatch exhibited the greatest sensitivity to annealing conditions. Isothermal anneals at low temperature (generating strong driving forces for precipitate formation) were found to produce plastic deformation via the formation of faulted dislocation loops and patterning was therefore rather limited. On the other hand,

careful optimization of the annealing temperature during the simulation was found not only to increase the patterning efficiency but also to inhibit the formation of faulted loops, resulting in optimally patterned samples. Calculations suggest that gradual segregation of the two components during variable temperature annealing reduces the maximum shear stresses within the film and at the same time also increases the stacking-fault energy, thereby inhibiting the formation of faulted loops. Additional effects related to the temperature dependence of other mechanical properties of the film may also play a role.

The results of this study suggest generically useful guidelines for selection of material systems and annealing conditions for the experimental realization of strain-directed phase segregation in simple fcc binary alloys. Future studies with material models that exhibit more complex phase diagrams will increase the application scope of this attractive approach for fabricating films with highly ordered structures that could be useful in a broad range of technologies.

ACKNOWLEDGMENTS

APPENDIX: CALCULATION OF ATOMIC STRESS

The atomic stress tensor $\sigma_i^{\alpha\beta}$ associated with atom i is given by[31]

$$\sigma_i^{\alpha\beta} = \frac{1}{(V/N)}\left[\frac{1}{2}\sum_{j\neq i}\frac{x_{ij}^{\alpha}x_{ij}^{\beta}}{r_{ij}}\frac{dE(r_{ij})}{dr_{ij}} - k_B T\delta_{\alpha\beta}\right], \tag{A1}$$

where V is the volume of the system, N is the total number of atoms in the system, x_{ij}^a is the α coordinate of the vector joining atoms i and j, r_{ij} is the distance between atoms i and j, and $E(r_{ij})$ is the interaction energy between atoms i and j, that is, here regarded as central; in the case of noncentral forces the formula for the stress is more complex. In Eq. (A1) the thermal contribution to the stress ($k_B T\delta_{\alpha\beta}$) results from the equipartition theorem. In order to calculate the local shear stress on a {111} plane in the relevant $\langle 112\rangle$ directions, which enters Eq. (12), the stress tensor at the position of atom i was taken as an average over atomic level stresses of i and neighboring atoms in a sphere of radius R centered at atom i. The averaging radius was chosen as the radius of the minimum critical loop defined in the main text, i.e., $R \sim 2\overline{a_0}$, where $\overline{a_0}$ is a representative lattice parameter.

Once the stress tensor is computed in Cartesian coordinates ($\boldsymbol{i},\boldsymbol{j},\boldsymbol{k}$), it is transformed to the coordinate system defined by the plane ({111}) of the faulted loop and the Burgers vector direction ($\langle 112\rangle$). For a cubic system, there are four {111} planes, and in each of them we can define an orthonor-

mal basis set that may be collectively represented by $\boldsymbol{i'} = 1/\sqrt{6}\langle 112\rangle$, $\boldsymbol{j'} = 1/\sqrt{2}\langle 110\rangle$, and $\boldsymbol{k'} = 1/\sqrt{3}\langle 111\rangle$. The transformation is then accomplished with the matrix

$$A = \begin{bmatrix} \boldsymbol{i}\cdot\boldsymbol{i'} & \boldsymbol{j}\cdot\boldsymbol{i'} & \boldsymbol{k}\cdot\boldsymbol{i'} \\ \boldsymbol{i}\cdot\boldsymbol{j'} & \boldsymbol{j}\cdot\boldsymbol{j'} & \boldsymbol{k}\cdot\boldsymbol{j'} \\ \boldsymbol{i}\cdot\boldsymbol{k'} & \boldsymbol{j}\cdot\boldsymbol{k'} & \boldsymbol{k}\cdot\boldsymbol{k'} \end{bmatrix}. \tag{A2}$$

Using the standard tensor transformation, the shear stress at atom i within the {111} plane acting in the $\langle 112\rangle$ direction is then given by

$$\tau_i^{13} = \sum_k \sum_l a_{1k}a_{3l}\sigma_i^{kl}, \tag{A3}$$

where a_{1k} and a_{3l} are corresponding elements of the matrix A given by (A2).

[1] M. Gao, J. Sun, E. Dulkeith, N. Gaponik, U. Lemmer, and J. Feldmann, Langmuir **18**, 4098 (2002).
[2] E. L. Bizdoaca, M. Spasova, M. Farle, M. Hilgendorff, and F. Caruso, J. Magn. Magn. Mater. **240**, 44 (2002).
[3] D. P. Long, J. L. Lazorcik, and R. Shashidhar, Adv. Mater. (Weinheim, Ger.) **16**, 814 (2004).
[4] F. Leroy, G. Renaud, A. Letoublon, R. Lazzari, C. Mottet, and J. Goniakowski, Phys. Rev. Lett. **95**, 185501 (2005).
[5] H. Brune, M. Giovannini, K. Bromann, and K. Kern, Nature (London) **394**, 451 (1998).
[6] C.-Y. Hung, A. F. Marshall, D.-K. Kim, W. D. Nix, J. S. Harris, Jr., and R. A. Kiehl, J. Nanopart. Res. **1**, 329 (1999).
[7] A. Ohtake and N. Koguchi, Appl. Phys. Lett. **89**, 083108 (2006).
[8] Z. Zhong, P. Chen, Z. Jiang, and G. Bauer, Appl. Phys. Lett. **93**, 043106 (2008).
[9] K. Pohl, M. C. Bartelt, J. de la Figuera, N. C. Bartelt, J. Hrbek, and R. Q. Hwang, Nature (London) **397**, 238 (1999).
[10] A. M. Nieves, V. Vitek, and T. Sinno, Appl. Phys. Lett. **93**, 191914 (2008).
[11] S. Zou, D. Maspoch, Y. Wang, C. A. Mirkin, and G. C. Schatz, Nano Lett. **7**, 276 (2007).
[12] T. R. Mattsson and H. Metiu, Appl. Phys. Lett. **75**, 926 (1999).
[13] R. F. Sabiryanov, M. I. Larsson, K. J. Cho, W. D. Nix, and B. M. Clemens, Phys. Rev. B **67**, 125412 (2003).
[14] Y. Lou and J. L. Bassani, J. Mech. Phys. Solids **56**, 3507 (2008).
[15] W. Lu and D. Kim, Acta Mater. **53**, 3689 (2005).
[16] J. Cahn and E. Hilliard, J. Chem. Phys. **28**, 258 (1958).
[17] P. L. Williams, Y. Mishin, and J. C. Hamilton, Modell. Simul. Mater. Sci. Eng. **14**, 817 (2006).
[18] B.-J. Lee and J.-H. Shim, CALPHAD: Comput. Coupling Phase Diagrams Thermochem. **28**, 125 (2004).
[19] D. A. Porter and K. E. Easterling, *Phase Transformations in Metals and Alloys* (Van Nostrand Reinhold, New York, 1981).
[20] M. S. Daw and M. I. Baskes, Phys. Rev. B **29**, 6443 (1984).
[21] Y. Mishin, M. J. Mehl, D. A. Papaconstantopoulos, A. F. Voter, and J. D. Kress, Phys. Rev. B **63**, 224106 (2001).
[22] M. I. Baskes, Phys. Rev. B **46**, 2727 (1992).
[23] B.-J. Lee, J.-H. Shim, and M. I. Baskes, Phys. Rev. B **68**, 144112 (2003).
[24] J. C. Gilbert and J. Nocedal, SIAM J. Optim. **2**, 21 (1992).
[25] M. R. Hitchcock and C. K. Hall, J. Chem. Phys. **110**, 11433 (1999).
[26] H. Mehrer, *Diffusion in Solids: Fundamentals, Methods, Materials, Diffusion-Controlled Processes* (Springer, New York, 2007).
[27] M. E. Thompson, C. S. Su, and P. W. Voorhees, Acta Metall. Mater. **42**, 2107 (1994).
[28] D. Y. Li and L. Q. Chen, Acta Mater. **46**, 2573 (1998).
[29] J. Friedel, *Dislocations* (Pergamon, New York, 1964).
[30] J. J. Gilman, *Electronic Basis of the Strength of Materials* (Cambridge University Press, New York, 2003).
[31] S.-P. Chen, T. Egami, and V. Vitek, Phys. Rev. B **37**, 2440 (1988).